Journal of Colloid and Interface Science 594 (2021) 409–423

Contents lists available at ScienceDirect

Journal of Colloid and Interface Science

journal homepage: www.elsevier.com/locate/jcis

Regular Article

A permeable on-chip microvasculature for assessing the transport of macromolecules and polymeric nanoconstructs

Maria Grazia Barbato [a,b], Rui C. Pereira [a,1], Hilaria Mollica [c], AnnaLisa Palange [a], Miguel Ferreira [a], Paolo Decuzzi [a,*]

[a] Laboratory of Nanotechnology for Precision Medicine, Fondazione Istituto Italiano di Tecnologia, Via Morego 30, 16163 Genoa, Italy
[b] Department of Informatics, Bioengineering, Robotics and System Engineering (DIBRIS), University of Genoa, Via Dodecaneso 25, 16146 Genoa, Italy
[c] I.R.C.C.S. Istituto Giannina Gaslini, Via Gerolamo Gaslini 3, 16147 Genoa, Italy

GRAPHICAL ABSTRACT

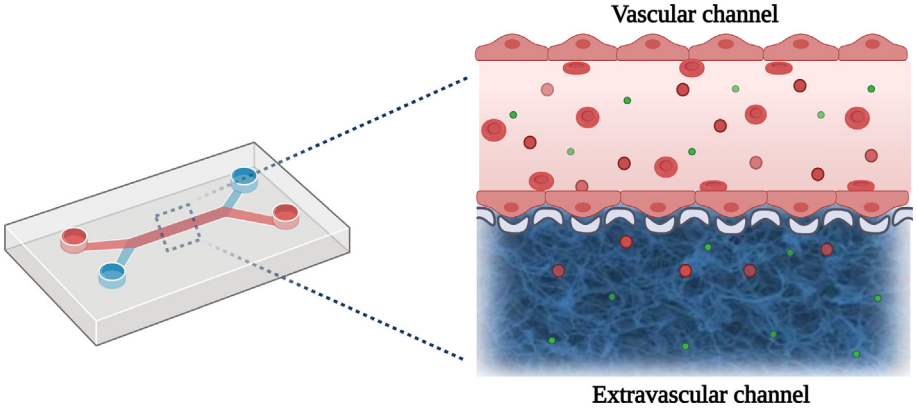

ARTICLE INFO

Article history:
Received 30 December 2020
Revised 23 February 2021
Accepted 9 March 2021
Available online 17 March 2021

Keywords:
Vascular adhesion
Nanoparticles
Permeability
Microfluidic

ABSTRACT

Hypothesis: The selective permeation of molecules and nanomedicines across the diseased vasculature dictates the success of a therapeutic intervention. Yet, *in vitro* assays cannot recapitulate relevant differences between the physiological and pathological microvasculature. Here, a double-channel microfluidic device was engineered to comprise vascular and extravascular compartments connected through a micropillar membrane with tunable permeability.

Experiments: The vascular compartment was coated by endothelial cells to achieve permeability values ranging from ~0.1 μm/sec, following a cyclic adenosine monophosphate (cAMP) pre-treatment (25 μg/mL), up to ~2 μm/sec, upon exposure to Mannitol, Lexiscan or in the absence of cells. Fluorescent microscopy was used to monitor the vascular behavior of 250 kDa Dextran molecules, 200 nm polystyrene nanoparticles (PB), and 1,000 × 400 nm discoidal polymeric nanoconstructs (DPN), under different permeability and flow conditions.

Findings: In the proposed on-chip microvasculature, it was confirmed that permeation enhancers could favor the perivascular accumulation of ~200 nm, in a dose and time dependent fashion, while have no effect on larger particles. Moreover, the microfluidic device was used to interrogate the role of particle

* Corresponding author.
E-mail address: paolo.decuzzi@iit.it (P. Decuzzi).

[1] Present address: Neurobiology of miRNA, Fondazione Istituto Italiano di Tecnologia, Via Morego 30, 16163 Genoa, Italy.

https://doi.org/10.1016/j.jcis.2021.03.053
0021-9797/

deformability in vascular dynamics. In the presence of a continuous endothelium, soft DPN attached to the vasculature more avidly at sub-physiological flows (100 μm/sec) than rigid DPN, whose deposition was larger at higher flow rates (1 mm/sec). The proposed double-channel microfluidic device can be efficiently used to systematically analyze the vascular behavior of drug delivery systems to enhance their tissue specific accumulation.

1. Introduction

The human vascular system has a remarkable ability to maintain tissue and cellular homeostasis in the body through a complex network of arteries, capillaries, and veins. The smallest vessels – the capillaries – are responsible for distributing nutrients and collecting waste from every single organ. As such, their walls comprise only the basal membrane and a monolayer of endothelial cells [1]. Transport across capillaries, from the vascular to the extravascular compartment, occurs via the paracellular pathway, exploiting openings at the interface among adjacent endothelial cells; and the transcellular pathway, using receptors and intracellular vesicles as shuttles to connect the two compartments. Depending on the vascular district and the biophysical properties of the agent to be transported – small molecules, macromolecules and nanoparticles – the transcellular pathway could be more relevant than the paracellular pathway [2,3]. For instance, the brain capillary network is characterized by very tight intra-endothelial cell junctions that limits the paracellular pathway in favor of a more selective transcellular transport, resulting in an overall modest vascular permeability [4–6]. On the other hand, capillaries in the kidneys, intestine, and liver – the liver sinusoids – are characterized by a discontinuous or even fenestrated endothelium that facilitates the paracellular transport, resulting into a high vascular permeability [7,8].

A variety of pathologies, including cancer, atherosclerosis, thrombosis, and, more in general, inflammatory diseases, are associated with alterations in vascular permeability [9,10]. For its dysregulated and chaotic growth, the cancer neovasculature presents a tortuous capillary network and large openings – fenestrations – that could range up to several hundreds of nanometers. This results in lower perfusion, and blood flow velocities, and higher vascular permeability as compared to healthy capillary networks [11,12]. Similarly, the inflamed vasculature is associated with more relaxed endothelial junctions to favor the recruitment of circulating monocytes and other cells of the immune system from the vascular network to the diseased tissue [13]. Incidentally, these alterations in vascular permeability have been extensively exploited to facilitate the passive accumulation of a variety of therapeutic agents at diseased sites. For instance, in cancer therapy, the Enhanced Permeability and Retention Effect (EPR) has been invoked over the last 20 years to design liposomes, polymeric and metal-based nanoparticles that could accumulate within the malignant tissue through the vascular fenestrations and remain in there because of the inefficient lymphatic drainage [12,14]. A similar approach has been also adopted in targeting atherosclerotic plaques and the hyperpermeable vascular network in the inflammatory bowel disease [13,15].

Traditionally, *in vitro* models such as the Boyden chamber and *in vivo* experiments have been used to assess the transport properties of macromolecules and nanoconstructs. However, trans-well membrane system (Boyden chamber) cannot replicate the complex *in vivo* tri-dimensional cell organization and flow conditions [16]. Animal models also present well-known ethical and technical limitations [17]. More recently, researchers have been generating functional, endothelial networks within microfluidic devices in order to accurately, yet effectively, study the transport of macromolecules and nanoconstructs under different controlled conditions [18–25]. However, most vascular systems developed so far comprise large channels, with a characteristic size much larger than 100 μm, which are well above that of arterioles and capillaries [19]. Also, microchannels formed in tridimensional gels upon the spontaneous organization of endothelial cells suffer of poor geometrical control and stability over time [26,27]. Indeed, these systems could be thought of as more authentic representations of a microvascular network, but the lack of control on geometry, and therefore flow, limits their use in systematic analyses. Furthermore, microfluidic systems have been realized with vertically arranged channels replicating a trans-well system. However, in general, these systems cannot be efficiently used to quantify vascular permeability of molecules and nanoparticles because transport occurs across different optical planes [13,23,28,29].

In this work, the vascular permeability of macromolecules and polymeric nanoconstructs, both rigid and deformable, is analyzed utilizing a tridimensional model of a human microvessel. This is realized in a so-called double-channel microfluidic device where the vascular compartment and the extravascular chamber lay on the same geometric plane. Cyclic adenosine monophosphate (cAMP), Mannitol, and Lexiscan were employed to modulate the vascular permeability from physiological to pathological conditions, demonstrating the full potential of the system. After assessing the integrity of the vascular endothelial barrier against the FITC-fluorescent Dextran macromolecules (250 kDa), the microfluidic device was employed to study the vascular transport, adhesion and permeability of 200 nm nanoparticles and 1,000 × 400 nm discoidal polymeric nanoconstructs.

2. Materials and methods

Chemicals, reagents, and cells. The following chemicals and reagents were used for the fabrication of the microfluidic chip: AZ5214E positive photoresist and the corresponding solvent AZ726MF from Microchem (Italy), Chrome etch 18 from OrganoSpezialChemie GmbH (Germany), *N*-Methyl-2-pyridone from Sigma-Aldrich (Italy) as PG Remover and 1H,1H,2H,2H-Perfluorooctyltrichloro-silane, 97% from Alfa Aesar (Germany). For the lithographic process, the following materials were employed: a laser-writing machine (DLW6000), an ICP-RIE (Si 500, Sentech Instruments GmbH, Germany) for the Bosh process, and a Plasma System (Gambetti, Italy) for oxygen plasma treatment. The soft lithography process was conducted using polydimethylsiloxane (PDMS) (Sylgard 182) from Corning (Italy), glass coversheets No. 1.5H from Deckalaser and biopsy punches with OD = 1 mm from Miltex (Italy). As endothelial cell model Human Umbelical Vein Endothelial Cell (HUVEC) from PromoCell (USA) were used and cultured in endothelial growth medium according to the manufacture's guideline. [3–4,5-dimethylthiazolyl)-2,5-diphenyltetrazolium bromide] (MTT) ≥ 97% from Sigma-Aldrich was used for viability experiment together with a microplate reader from Tecan (CH). For integrating the vasculature on the microfluidic chip, the following reagents were used: collagen type I solution (≥95%) from bovine skin and Human Fibronectin from Sigma-Aldrich and Matrigel© High Con-

centration from Corning. Permeability experiment were performed by using the following reagents and instruments: 250 kDa FITC-Dextran (0.5 μg/mL) from Sigma-Aldrich, Fluoresbrite® YO Carboxylate Microspheres 200 nm (2.27×10^9 particles/mL) from Polysciences (USA), a syringe pump model Harvard Pump 11 Elite from Harvard Apparatus (USA), a multirack syringe pump model 230 from K_d Scientific (USA), polyethylene tubes (BTPE-50, ID = 0.58 mm, OD = 0.97 mm) from Instech Laboratories (Germany) and an *epi*-fluorescent inverted microscope from Leica (Germany) model Leica 6000 (objective 10×, 0.22 N.A.). For modulating the permeability of the endothelial barrier, the following reagents were used: N^6,2′-O-Dibutyryladenosine 3′,5′-cyclic monophosphate sodium salt (db-cAMP) (≥98.5%), Mannitol (≥98%) and Lexiscan (≥98%) from Sigma-Aldrich. In order to characterize the vasculature in the microfluidic device the following instruments were employed: Scanning Electron Microscope JSM-6490LV from FEI Company (USA), a Critical Point Drier (CPD) K850WM (UK) and a sputter coater model 550 from Emitech (Italy), and an A1-Nikon Confocal Microscope from Nikon Corporation (Japan). For immunofluorescence staining protocols, the following antibodies and reagents were used: PFA 4% from Santa Cruz Biotechnologies (USA), Ms anti-human VE-Cadherin (1:200), AlexaFluor 488 anti-mouse secondary antibody (1:500) from Abcam (UK), Hoechst (1 mg/mL) (1:1000) and AlexaFluor 488 Phalloidin from Invitrogen (USA).

Microfluidic device fabrication. Double-channel microfluidic device was fabricated *via* two lithographic steps, as previously reported by the authors with some modifications [30]. Briefly, using a laser-writing machine, a negative optical mask for the two-parallel channels and a positive optical mask for the micropillars membrane were realized. In the first step, the AZ5214E photoresist was used as a positive photoresist and spin-coated at 4,000 rpm on a Cr surface. The sample was then baked a 110 °C for 60 s to clean the resist. The mask including the micropillars was impressed using a mask-aligner on the resist at 80 mJ. To develop the resist, the solvent AZ726MF was used. The impressed pattern was transferred from the resist to the Cr mask by using a Cr etchant. The residual resist layer was then removed from the unexposed surface via PG remover at 80 °C for five minutes and a cleaning step procedure with ultrapure water. An ICP-RIE Bosh process was performed to dig the micropillar membrane over the Si etching down by 5 μm. The obtained Si wafer with the impressed micropillar membrane was used in the second step in order to transfer the channels. In this second step, the AZ5214E was used as negative photoresist. AZ5214E was spin-coated on the residual Cr layer and baked at 110 °C for 60 s. Subsequently, the channels mask was aligned on the micropillar membrane and then exposed at 95 mJ. Because the resist was used in the reversal mode, the wafer required an additional baking phase at 120 °C for 120 s and an exposure phase at 300 mJ. The development was performed as for the micropillars. A second ICP-RIE Bosh etching was performed down to 50 μm, the actual, final height of the channels, in order to get both pillars and channels on the Si layer. At the end of the lithographic process, the silicon template was covered with a layer of silanes by using a desiccator for 1 h. The PDMS replica were obtained by mixing base and curing agent in a ratio 1:10 (w/w). The PDMS solution was casted on the silicon template, degassed until all bubbles were removed and cured at 80 °C overnight. The PDMS replicas were cleaned with a scotch-tape and inlet and outlet ports were created with a biopsy punch. Before bonding the PDMS to a glass coversheet, the PDMS replicas were autoclaved (dry autoclave) and dried at 80 °C for 4 h. In addition, also the glass cover sheets were autoclaved and dried in order to get the same temperature of PDMS replicas and prevent collapse of the micropillars structure during the bonding step. Oxygen (O_2) plasma treatment (pressure = 1.0 mbar, power = 20 W, time = 20 s) was performed and PDMS replicas were bonded to the glass coversheets. The obtained microfluidic chip had a rectangular cross section of 210 μm (width), a height of 50 μm and a port-to-port length of 2.7 cm. The micropillar membrane, positioned in the middle part of the channels, had a length of 500 μm and a width of 25 μm, with a gap-size between pillars of 3 μm.

Extracellular matrix realization. To mimic the extravascular space, different extracellular matrices (ECM) were realized by mixing increasing amount (vol/vol) of Matrigel with a solution of type I collagen. Starting from a stock solution of collagen type I (6 mg/mL), a final collagen concentration of 2 mg/mL was obtained by using deionized water, 10x EMEM, HEPES buffer 1 M and 1 M NaOH solution. Seven different types of ECM were prepared, starting from 100% of collagen type I and then adding increasing volumes of Matrigel (i.e., 10, 20, 30, 50, 95%) up to 100% of Matrigel. During the matrix manufacturing process, all components were kept at 4C to avoid matrix polymerization. In order to characterize the ultrastructure, the obtained composite matrices were placed in a petri dish and allowed to polymerize in an incubator for at least 30 min (37 °C, >95% humidity).

Extracellular matrix characterization: Scanning Electron Microscopy (SEM). Matrix ultrastructure was analyzed using a scanning electron microscope. Samples of the selected matrix composition were fixed in 2% glutaraldehyde in 0.1 M sodium cacodylate buffer, pH 7.3 for 2 h at room temperature, and then post-fixed in 1% OsO_4 phosphate buffer for two hours. Then, samples were dehydrated through an ascending series of ethanol solutions (30 up to 100%), and critical point dried for 1 h using CO_2. The obtained matrices were sputter-coated with 10 nm of gold, and multiple images were acquired with an accelerating voltage of 10 kV and a magnification of 5,000×. To characterize the structural features of the 3D matrix network, SEM images were analyzed using the free software ImageJ. The porosity of the ECM was quantified by using three independent images from each sample, binarizing them and calculating the areas of black (pores) over the white (fibers) pixels, within the binary images.

Extracellular matrix characterization: diffusion study. Microfluidic devices were autoclaved at 120 °C for sterilization (wet autoclave) and then dried overnight (>15 h) at 80 °C. Before extracellular matrix filling, microfluidic devices were stored for 1 h at 4 °C. During the whole procedure, matrix solutions were kept on ice. At this point, 10 μL of the selected matrix were introduced into the extravascular channel and loaded devices were transferred at 37 °C for 30 min to allow matrix gelation. To characterize the transport of biomolecules within the extracellular matrix, 250 kDa FITC-Dextran (0.5 μg/mL) and Fluoresbrite® YO Carboxylate Microspheres 200 nm (2.27×10^9 particles/mL) were used. The avascular channel was connected to a syringe pump *via* polyethylene tubing. For all the experiments, the working solutions were infused in the avascular channel at a volumetric flow rate of 100 nL/min. Dextran or 200 nm beads were infused through the inlet port, allowing to fill completely the avascular channel before starting the time-lapse fluorescence acquisition (5 s intervals *via* an *epi*-fluorescent inverted microscope). Time-lapse images were analyzed using ImageJ software, selecting Regions of Interest (ROI) in the avascular and extravascular channels. When the avascular channel was fully filled with the solution, the permeability coefficient P was calculated as, readapting the equation reported in [23,30]:

$$P = \frac{A_{ECM} \cdot \left(\frac{I_f - I_i}{\Delta t}\right)}{w_{pillars} \cdot \left(I_{vascular} - I_{pillars}\right)_{t=0}}$$

where A_{ECM} refers to the surface area of the ROI within the extravascular space; I_f is the total fluorescence intensity of the extravascular region at the final time and I_i at t = 0; $w_{pillars}$ is the width of the pil-

lars across which diffusion occurs; $I_{vascular}$ is the total fluorescence intensity of the vascular channel once completely filled and $I_{pillars}$ is the total fluorescence intensity of the interface between the vascular region and the ECM region, both at t = 0. Δt is the time interval between t = 0 and the final time of the experiment.

Vascular endothelium in the microfluidic device. To mimic the extravascular compartment, a 80% collagen type I – 20% Matrigel matrix was selected. Next, the vascular channel was filled with 50 μg/mL of a human fibronectin solution and incubated for 2 h at 37 °C. HUVEC were cultured till confluence (~80%) and then trypsinized, counted and concentrated to 5×10^6 cells/mL. Cells were used until passage 6 (P6). For complete coverage of the PDMS walls, a double seeding procedure was used. In the first step, 10 μL of cell suspension was added through the inlet port of the vascular channel and immediately the microfluidic chip was faced upside-down to promote endothelial cells adhesion to the top of the channel. In this configuration, microfluidic chips were incubated at 37 °C, 5%CO_2 for 1 h. A second cell-seeding step was performed, without flipping the microfluidic chip, allowing the adhesion of the endothelial cells to the bottom of the channel. Devices were incubated at 37 °C for 2 h. Micropipette tips, filled with 200 μL of culture media, were connected to inlet ports of the vascular channel, while empty tips were placed in the correspective outlets. The inlet and outlet ports of the extravascular channel were connected with tips filled with 50 μL of culture media. Cell culture medium was changed every 12 h. HUVEC were cultured to reach confluence (approximately 2 days) in order to form a continuous monolayer before conducting permeability experiments.

db-cAMP treatment to tune the vascular permeability. In order to strengthen, the endothelial barrier, HUVEC were treated with increasing concentrations of N^6,2′-O-Dibutyryladenosine 3′,5′-cyclic monophosphate sodium salt (db-cAMP). After 2 h from the cells seeding, endothelial cells were treated until confluence with 25, 50, 100 or 200 μg/mL of db-cAMP, respectively. Due to the reduced paracellular permeability observed, in the following experiments HUVEC were cultured with 25 μg/mL of db-cAMP.

Endothelial cells viability. To assess the effect of db-cAMP on HUVEC viability and proliferation, an MTT assay was performed. The assay detects the reduction of MTT by mitochondrial dehydrogenase to blue formazan product. Briefly, 10^5 cells/well were seeded in 96-well plates and incubated at 37°C, 5% CO_2, for 24 h. Next, the medium was replaced with Endothelial Cell Growth Medium containing the corresponding concentrations of db-cAMP (25, 50, 100 and 200 μg/mL). After 24, 48 and 72 h of incubation, the MTT solution (5.0 mg/mL PBS) was diluted in Endothelial Cell Growth Medium (0.25 μg/mL), added to each well and incubated at 37°C for 4 h. The resulting formazan crystals were dissolved by adding ethanol (200 μL/well), and the absorbance was read at 570 nm using a microplate reader. Controls (i.e., cells that had received no treatment) were normalized to 100% and readings from treated cells were expressed as the percentage of viability inhibition. Five replicates were considered for each data point.

Mannitol and Lexiscan treatment to tune the vascular permeability. For modeling the opening of the vascular endothelium, Mannitol 1 M was infused in the vascular channel for 5, 15 and 30 min after achieving cell confluence. 1 μM of Lexiscan was infused into the vascular channel and permeability calculated after 5, 15, and 30 min of treatment. Permeability analyses were conducted as previously reported.

Discoidal polymeric nanoconstructs (DPN) permeability and adhesion study. Discoidal polymeric nanoconstructs (DPN) were synthesized by employing a top-down fabrication process, as already reported by the authors [31-34]. For the experiments, two types of DPN were fabricated, soft, deformable DPN (sDPN) and rigid DPN (rDPN). Briefly, a polymeric mixture composed by poly(lactic-*co*-glycolic acid) (PLGA) and polyethylene glycol (PEG) was casted in the wells of the sacrificial PVA template and exposed to UV-light for polymerization. PVA templates were dissolved in water and particles collected through centrifugation. Lipid Rhodamine B (Avanti Polar Lipids, USA) was added to the polymeric paste composing DPN for permeability experiments, while Lipid-Cy5 synthetized by the authors was used for adhesion experiments [35]. On day two post seeding, the permeability of HUVEC monolayers to both DPN configurations (500×10^6 particles/mL) was tested as reported previously. For the adhesion study, a multirack syringe pump was placed inside a cell incubator and loaded with 1 mL syringes. The vascular channel was perfused with sDPN and rDPN (50×10^6 particles/mL) with and without endothelial cells at 0.1 μL/min (0.2 dyne/cm^2), 0.25 μL/min (0.7 dyne/cm^2) and 0.5 μL/min (1 dyne/cm^2), corresponding to the tumor flow rate, an intermediate flow rate and physiological flow rate, respectively [36]. Channels were then flushed with culture medium to remove non-adhering particles and fixed with 4% PFA for 15 min. Nanoconstructs adhesion was immediately investigated using an A1-Nikon confocal microscope.

Electron Microscopy Imaging. Vascularized microfluidic chips were imaged *via* scanning electron microscopy. Cells in the vascular channels were fixed in 2% glutaraldehyde in 0.1 M sodium cacodylate buffer, pH 7.3 for 1 h at room temperature. Subsequently, the PDMS chips, with endothelial cells adhered to the channel walls, were detached from the glass coversheets and post-fixed in 1% OsO_4 phosphate buffer for two hours. The samples were then dehydrated through ascending series of ethanol solutions (30% up to 100%), followed by a solution of 1:1 ethanol:hexamethyldisilazane (HMDS, ≥99% Sigma-Aldrich), and 100% HMDS and dried overnight at room temperature. The obtained microfluidic chips were sputter-coated with 10 nm of gold and images acquired with accelerating voltage of 10 kV.

Cells immunofluorescence staining. Endothelialized vascular channels were fixed with 4% of PFA for 20 min at room temperature. Following fixation, channels were washed three times with cold PBS, permeabilized with a solution of Triton X 0.3% in PBS for 15 min and incubated with 20% of goat serum solution diluted in PBS for 1 h at 4 °C. Endothelial Cadherins were targeted with antihuman VE-cadherin antibody overnight at 4 °C with 10% of goat serum. The unbound antibody was removed with three washes of cold PBS. After that microfluidic chips were incubated with a solution of Alexa Fluor 488 anti-mouse secondary antibody (1:500) with 10% of goat serum for 2 h at 4 °C. Cells were washed again three times with cold PBS and incubated with a solution of PBS and 1:1000 Hoechst for 30 min at room temperature. F-actin cytoskeleton was stained in green using Alexa Fluor™ 488 Phalloidin according to the supplier instructions. Images were acquired using an A1-Nikon confocal microscope

Statistical analysis. All data are presented as the mean ± SD using GraphPad Prism5 software. Calculation of porosity was analyzed via 1-way ANOVA. p – values < 0.05 were denoted with *, p – value < 0.01 with **. Permeability studies and DPN adhesion studies were evaluated via 2-way ANOVA analysis of variance followed by *ad hoc* Bonferroni post-test. p – values < 0.05 were denoted with *, p – values < 0.01 with **, and p – values < 0.001 with ***. For all experiments, at least 5 independent repetitions were conducted.

3. Results

Architecture of the double-channel microfluidic device: the vascular compartment. A soft-lithographic approach was employed to create an optically-clear poly(dimethyl siloxane) (PDMS) double-channel microfluidic device (Fig. 1**A**), following previous works by the authors [22,30].

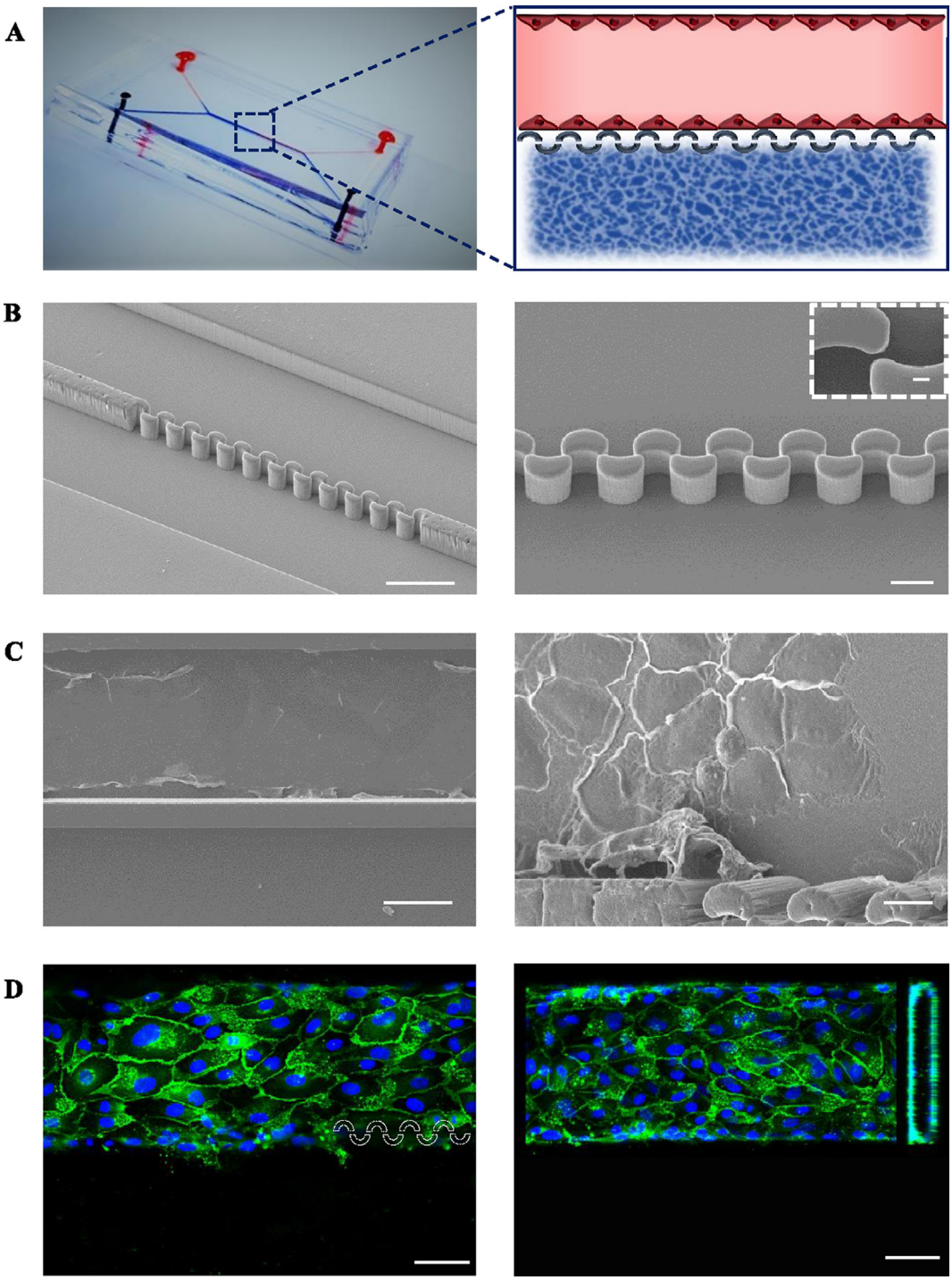

Fig. 1. The double-channel microfluidic device – the vascular compartment. **A**. Photograph (left) and schematic illustration (right) of a double-channel microfluidic device showing the vascular channel (reddish color) and the extravascular chamber (bluish color). **B.** Scanning electron micrographs showing the double-channel microfluidic structure (left) and the micropillars geometry (right) (Scale bar: 100 μm. Inset – Scale bar 5 μm). **C.** Scanning electron micrographs of the vascular channel (left) and its micropillar membrane (right) covered by endothelial cells (Left – Scale bar: 100 μm. Right – Scale bar: 20 μm). **D.** Immunofluorescence images of a continuous layer of human umbilical vascular endothelial cells (HUVEC) covering the vascular compartment. (Nuclei – blue; VE-cadherin molecules – green). On the right, cross-sectional view of the endothelialized channel. (Scale bar: 100 μm). (For interpretation of the references to color in this figure legend, the reader is referred to the web version of this article.)

The microfluidic device is composed of two parallel channels interconnected in the central section via an array of micropillars, realizing a permeable membrane (Fig. 1**B**). Specifically, this central permeable section has a characteristic length of 500 μm and an inter-pillar gap size of ~3 μm, as detailed by the scanning electron micrograph shown in the right inset of Fig. 1**B**. Such a configuration realizes a physical separation between the two channels supporting the identification of the two different biological compartments – the vascular and the extravascular space – without hampering the transport of molecules, nanoparticles and cells. To build a physiologically relevant and vascularized organ-on-chip, the upper channel was designed to accommodate endothelial cells (the vascular compartment) while the bottom channel was filled with

extravascular matrix components (the extravascular compartment).

Human umbilical vein cells (HUVEC) were cultured in the vascular compartment over a fibronectin-coated PDMS surface and let to spread, grow and stably adhere, as documented in Fig. 1**C**. Specifically, HUVEC were seeded in the upper channel after treating the PDMS surface with 50 μg/mL of human fibronectin for 2 h. A double-step cell seeding procedure was employed to entirely cover the walls of PDMS channel. After fibronectin coating, HUVEC were gently pipetted into the vascular channel, and the microfluidic chip was immediately flipped. In this configuration, HUVEC were left to adhere to the top surface of the channel for 1 h, at 37 °C. Then, the microfluidic chip was flipped again, HUVEC were pipetted into the vascular channel in order, this time, to cover the bottom surface. A detailed analysis with confocal fluorescence microscopy revealed the formation of a continuous endothelial monolayer covering the bottom, top and later walls of the vascular compartment even next to the pillar membrane (Fig. 1**D**). The right inset of Fig. 1**D** also shows a lateral projection of the confocal microscopy images demonstrating that the endothelial cells uniformly coat the vascular compartment's surface along its entire rectangular cross section. Moreover, the staining of the VE-Cadherin proteins (green) demonstrates the formation of inter-endothelial cell junctions that are important regulators of vascular integrity and permeability (Fig. 1**D**).

Architecture of the double-channel microfluidic device: the extravascular compartment. On the other side of the micropillar membrane, the extravascular compartment was filled with components of the extracellular matrix (ECM), including Matrigel and Collagen type I.

To finely modulate the ECM permeability, the relative ratio between the two components was varied from 100% Matrigel (8.6 mg/mL) to 100% Collagen (2 mg/ml) realizing seven different matrix configurations (see table in Fig. 2**A**). Representing scanning electron microscopy images of four matrix configurations are shown in Fig. 2**B**, specifically for the case of 100% Collagen (**left**); 80% Collagen and 20% Matrigel; 50% Collagen and 50% Matrigel; 100% Matrigel (**right**). This series of images qualitatively shows that the progressive increase in Matrigel content is associated with a decrease in matrix permeability. The first image on the left, which is associated with a Collagen only matrix, shows fibrils arranged to form pores over multiple scales and certainly comparable in size to that of a cell. As the Matrigel content increases, the Collagen fibers appear to entangle more forming denser structures. At 20% (v/v) Matrigel, the gel is composed of thicker fibers still preserving the original porosity of the network. At 50% (v/v) Matrigel, the collagen fibers are compacted into a dense matrix with a drastically reduced network porosity as compared to the previous configurations. Finally, the first image on the right, which is associated with a Matrigel only matrix, shows a continuous network in which individual pores and fibers cannot be anymore distinguished at the considered magnification. The electron microscopy images were further analyzed using ImageJ to extract quantitative information on the matrix porosity

(**Supporting Fig. S1**). Fig. 2**B** shows the porosity variation as the Matrigel content in the extracellular matrix increases.

As expected, the porosity of the hydrogel reduces from 51 ± 4.6% for a Collagen only matrix to 2 ± 1.04% for a Matrigel only matrix. It is here important to highlight that SEM images, and the corresponding porosity analyses, were obtained on dehydrated matrices, as required by the imaging technique.

To investigate further the gel porosity in an actual functional assays, permeability studies were conducted on the seven matrix configurations using two different fluorescent tracers, namely the 250 kDa FITC-Dextran (green) and 200 nm polystyrene beads (red). These tracers were infused from the vascular compartment and observed as they slowly permeate the extravascular space (**Supporting Movies 1–6**). Dynamic Light Scattering (DLS) analyses of the two tracers returned a hydrodynamic diameter of 12.86 ± 3.74 nm for the Dextran molecules and 181 ± 31 nm for the beads (**Supporting Fig. S2**). The estimated permeability values are given in Fig. 2**C** and confirm that, for both tracers, the gel permeability drops progressively with the Matrigel content. Indeed, the permeability associated with the larger 200 nm polystyrene beads is overall smaller than that registered for the ~10 nm Dextran molecules. A rapid decrease in permeability is observed between 20 and 30% of Matrigel content. For higher Matrigel contents, the permeability of the 200 nm polystyrene beads goes to zero whereas it plateaus around ~0.2 μm/sec for the Dextran molecules. Based on these observations and data from the current literature [25,37], an extracellular matrix with a 20% Matrigel content was selected for the extravascular compartment of the microfluidic chip to recapitulate the ECM composition through fibrillar collagen type I and proteins associated with Matrigel. This matrix configuration offers a proper balance between molecule and particle permeability, while ensuring that the extravascular compartment is enriched with unique growth factors for cell culture.

Reducing the vascular permeability to circulating agents. The integrity of the endothelial barrier across the micropillar membrane was tested using the same two fluorescent tracers adopted for the ECM characterization.

The tracers were slowly infused through the vascular compartment and their permeation into the extravascular space was assessed via fluorescent microscopy in the absence (−HUVEC) and presence (+HUVEC) of endothelial cells. From the post-processing of the fluorescent microscopy acquisitions, reported in the **Supplementary Information** as **Supporting Movie 2**, it resulted that the 250 kDa FITC-Dextran molecules would readily flow across the micropillar membrane returning a permeability of 1.35 ± 0.3 μm/sec. The formation of a continuous monolayer of endothelial cells (+HUVEC) significantly reduced this permeability value to 0.93 ± 0.30 μm/sec (**Supporting Movie 7**), thus confirming the presence of a functional, vascular barrier (Fig. 3**A**). For the 200 nm beads, the permeability value in the absence of HUVEC was 0.88 ± 0.18 μm/sec and reduced dramatically to 0.04 ± 0.005 μm/sec in the presence of HUVEC (Fig. 3**A, Supporting Movie 9**). Importantly, in the absence of HUVEC, the permeability of the Dextran molecules and 200 nm beads into the extravascular space are comparable. However, the addition of HUVEC induces a much larger decrease in permeability for the 200 nm beads as opposed to the 10 nm macromolecules, resulting in a 30% vs 95% reduction, respectively. This demonstrated the size-dependent selectivity of the micropillar membrane.

To further modulate the permeability of the endothelial layer, cells were treated with Dibutyryl-cAMP (db-cAMP). This is an activator of cAMP-dependent protein kinases that is known to reduce vascular permeability by inducing changes in the endothelial cell–cell junctional proteins, like VE-cadherin [38]. Endothelial cells were treated with db-cAMP, ranging from 25 to 200 μg/mL, and tested for the permeability to 250 kDa FITC-Dextran molecules. A 3-fold decrease in permeability was observed already at 25 μg/mL db-cAMP, from 0.93 ± 0.30 to 0.27 ± 0.24 μm/sec (Fig. 3**A** and **Supporting Movie 8**). Similar permeability values were reported at higher db-cAMP concentrations (**Supporting Fig. S3A**). Moreover, cell viability studies showed that treating endothelial cells with 25 μg/mL db-cAMP did not induce any significant toxicity up to 72 h. On the other hand, some moderate toxicity returning a cell viability of ~70% was documented at the higher db-cAMP concentrations and longer incubation times (**Supporting Fig. S3B**). For this reason, all the experiments were conducted by culturing endothelial cells with 25 μg/mL db-cAMP. Note also that, not surprisingly, the reduction in permeability observed for the

A

Extracellular matrix		Protein concentration		
Collagen % (v/v)	Matrigel % (v/v)	Collagen [mg/mL]	Matrigel [mg/mL]	Total [mg/mL]
100%	-	2	-	2
90%	10%	1.8	0.86	2.66
80%	20%	1.6	1.72	3.32
70%	30%	1.4	2.58	3.98
50%	50%	1	4.3	5.3
5%	95%	0.1	8.17	8.27
-	100%	-	8.6	8.6

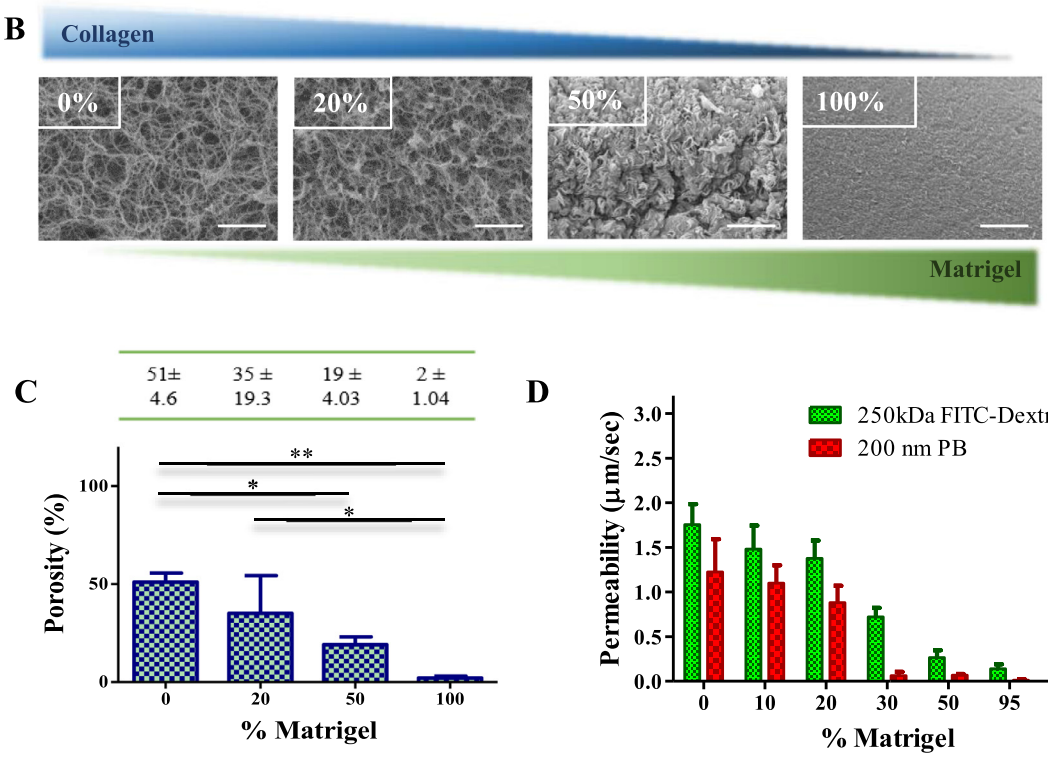

Fig. 2. The double-channel microfluidic device – the extravascular compartment. A. List of collagen type I and Matrigel concentrations used for the biologically derived extracellular matrix. B. Scanning electron micrographs of the tested extracellular matrices (Scale bar: 5 μm. $p < 0.05$ denoted with *, $p < 0.01$ denoted with **). C. Porosity percentage calculated via ImageJ analysis (n = 3). D. Diffusion of 250 kDa-FITC Dextran and 200 nm PB within the extracellular matrix ($n \geq 5$).

~10 nm FITC-Dextran molecules was not recapitulated for the larger 200 nm polystyrene beads. For these larger agents, a dramatic reduction in vascular permeability was already documented with the sole addition of the HUVEC. The pre-treatment with 25 μg/mL db-cAMP returned a permeability of 0.05 ± 0.04 μm/sec, which is statistically similar to the untreated case (0.04 ± 0.005 μm/sec – $p = 0.6890$).

Confocal images of endothelial cells treated with 25 μg/mL of db-cAMP documented a higher density of VE-cadherin proteins (green) as compared to the untreated case (Fig. 3**C**), further confirming the generation of tighter inter-endothelial bonds.

Increasing the vascular permeability to circulating agents. In drug delivery and biomedical imaging, the transient and reversible opening of the blood vessel walls is key to support the accumulation of molecules and nanocarriers in the diseased tissue. There-

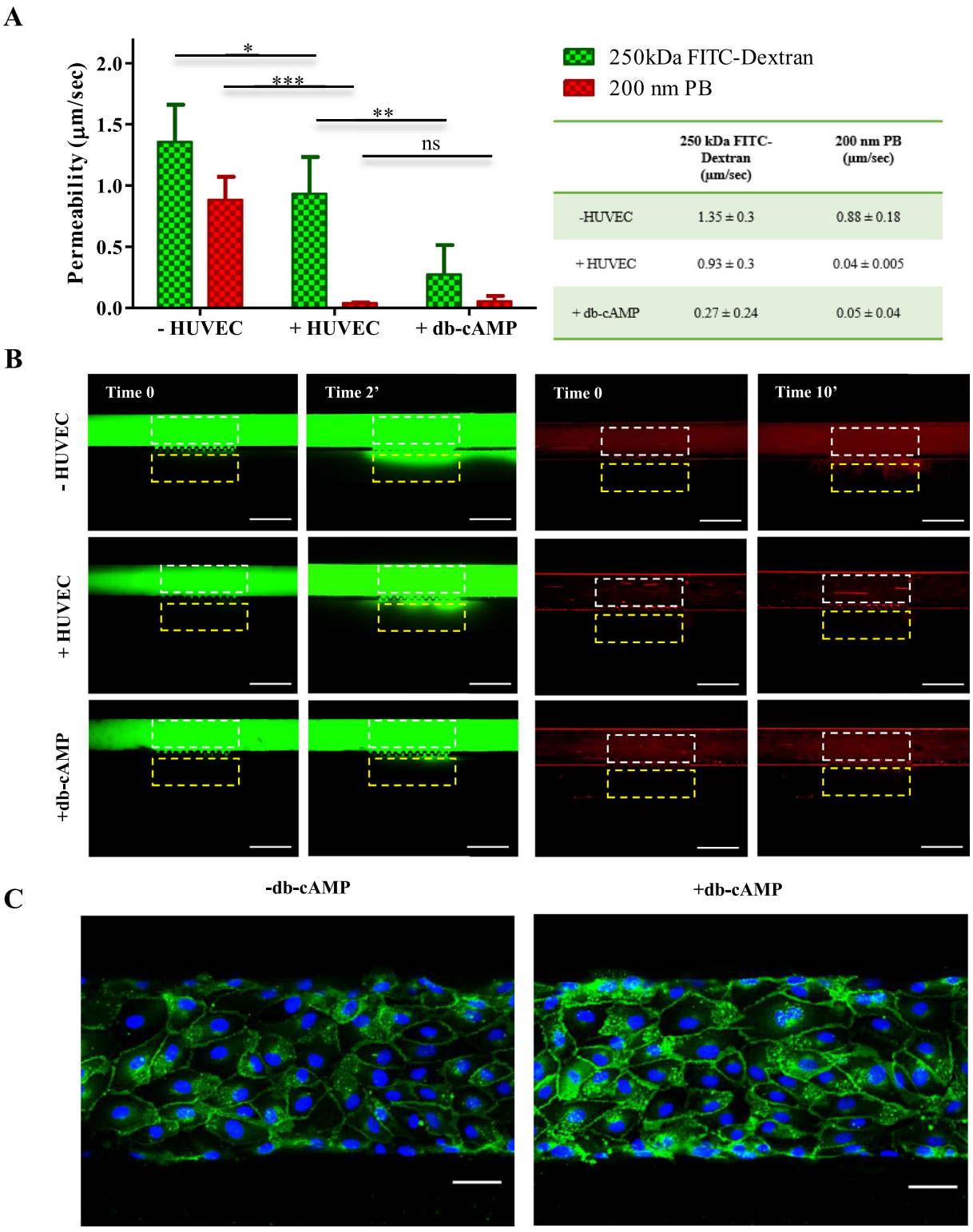

	250 kDa FITC-Dextran (µm/sec)	200 nm PB (µm/sec)
-HUVEC	1.35 ± 0.3	0.88 ± 0.18
+ HUVEC	0.93 ± 0.3	0.04 ± 0.005
+ db-cAMP	0.27 ± 0.24	0.05 ± 0.04

Fig. 3. Modulating vascular permeability. **A.** Permeability coefficients calculated for 250 kDa-FITC Dextran and 200 nm PB in a microfluidic device without HUVEC (−HUVEC), with HUVEC (+HUVEC), and with HUVEC pre-treated with 25 µg/mL of db-cAMP (+db-cAMP) ($n \geq 5$). ($p < 0.05$ denoted with *, $p < 0.01$ denoted with **, $p < 0.001$ denoted with ***). Permeability values are presented in the table as average ± SD. **B.** Representative fluorescence images of 250 kDa-FITC Dextran (left) and 200 nm PB (right) permeation at 0.1 µL/min across the micro-pillar membrane without endothelial cells (−HUVEC), with endothelial cells (+HUVEC) and with db-cAMP pre-treated endothelial cells (+db-cAMP) (Scale bar: 250 µm). **C.** Immunofluorescence images of VE-Cadherin molecules (green) on HUVEC before and after treatment with 25 µg/mL db-cAMP (Scale bar: 50 µm). (For interpretation of the references to color in this figure legend, the reader is referred to the web version of this article.)

fore, to further characterize the functionality of the vascular endothelium in the microfluidic chip, two different permeation enhancers were considered, namely Mannitol and Lexiscan.

The first agent, Mannitol, is clinically used to reduce excessive intra-tissue pressure, especially in the brain as its application causes on osmotic shrinkage of the endothelial cells and enhances

the BBB permeability [39]. In accordance with other studies, a 1 M Mannitol solution was infused into the vascular compartment under physiological conditions (37 °C, 5% CO_2, >95% of humidity) for 5, 15 and 30 min. Then, the permeability of the endothelial layer was assessed, following the same protocol described above, by infusing 250 kDa FITC-Dextran molecules and 200 nm polystyrene beads at 0.1 μL/min (Fig. 4**A**). The osmotic opening of the endothelial layer resulted in an increased, time-dependent extravascular accumulation for both 250 kDa FITC-Dextran molecules and 200 nm beads (**Supporting Movie 10, 11**). For the Dextran molecules, the permeability values (+HUVEC and + db-cAMP) increased from 0.27 ± 0.24 to 0.56 ± 0.10 μm/sec, to 0.78 ± 0.09 μm/sec and 0.99 ± 0.06 μm/sec after 5, 15 and 30 min of mannitol continuous infusion, respectively (Fig. 4**A**). A 30-minutes treatment with Mannitol would increase the permeability by over 3 times. Notice that in the absence of HUVEC, the permeability of Dextran was equal to 1.37 ± 0.2 μm/sec indicating that the Mannitol treatment is almost equivalent to transiently removing the endothelial layer. For the 200 nm beads, the permeability values (+HUVEC and + db-cAMP) increased from 0.029 ± 0.01 to 0.06 ± 0.02 μm/sec, 0.15 ± 0.01 μm/sec and 0.20 ± 0.006 μm/sec after 5, 10 and 30 min of mannitol treatment, respectively (Fig. 4**A**). This results in a 10-fold increase in the accumulation of 200 nm beads into the extravascular compartment (Fig. 4**C**).

Despite multiple successes with mannitol, the non-uniform effect among different brain regions and negative side effects (e.g., epileptic seizure) has limited the clinical application of this procedure [40]. A more recent approach is based on the manipulation of the Adenosine Receptors (AR) using the FDA-approved A_{2A} AR agonist (Lexiscan®). As with Mannitol, Lexiscan modulates cytoskeletal organization reflecting a down-regulation of both adherent and tight junctions [41,42]. In the proposed microfluidic device, a Lexiscan treatment (1 μM) was conducted as per the Mannitol. For 250 kDa FITC-Dextran, a plateau in permeability was already reached at 15 min of treatment returning a value of 0.64 ± 0.09 μm/sec (**Supporting Movie 12**). At 30 min of treatment, the permeability slightly but not significantly decreased down to 0.54 ± 0.23 μm/sec (p = 0.5124) (Fig. 4**B**). Thus, for dextran macromolecules, the infusion of Lexiscan induced an overall 2-fold increase in vascular permeability. A similar trend was also observed for the 200 nm beads for which a plateau was reached after 15 min of treatment with a permeability value of 0.24 ± 0.01 μm/sec (Fig. 4**B, Supporting Movie 13**). No change in permeability was documented at the longer treatment time of 30 min. However, differently from the 250 kDa FITC-Dextran, this was still sufficient to realize a 10-fold increase in vascular permeability. Indeed, no significant statistical difference was observed in terms of enhanced permeabilization for the 200 nm beads with Lexiscan or Mannitol.

The effect of the two vascular permeabilizers on the expression of VE-Cadherins and the organization of the actin cytoskeleton was then analyzed, as reported in the **Supporting Information**. The exposure of endothelial cells to hyperosmotic agents – Mannitol – resulted in the detachment of adjacent cells as documented by the drop in VE-cadherin expression already after just 5 min of treatment (**Supporting Fig. S4A**). A similar behavior was also documented with Lexiscan (**Supporting Fig. S4B**). However, in the case of Lexiscan, the opening of endothelial barrier is reversible and at 30 min of treatment, VE-Cadherin proteins started to appear again on the cell membrane and reassemble to form new intracellular bonds (**Supporting Fig. S4B**). These results confirm the enhanced paracellular permeability observed within the first minutes of Lexiscan treatment but also document the reversibility of the process.

Assessing the vascular dynamics of circulating polymeric nanoconstructs. The proposed microfluidic device can be used to study the transport of blood-borne nano- and micro-particles from the vascular to the extravascular compartments. In this context, three different types of particles were tested and compared: 200 nm polystyrene beads (PB), soft discoidal polymeric nanoconstructs (sDPN), and rigid discoidal polymeric nanoconstructs (rDPN). DPN are disc shaped nanoconstructs, with a 1,000 nm diameter and 400 nm height, and are fabricated following a soft lithography templating technique (Fig. 5**A-B**) [31–34]. These particles result from mixing together the biocompatible and biodegradable polymers, poly (lactic-*co*-glycoli acid) (PLGA) and polyethyleneglycol diacrylate (PEG-DA). Previous studies have shown that the mechanical stiffness of these particles can be modulated by tailoring the content of PEG-DA in the formulation [32]. First, vascular permeability experiments were carried out with soft and rigid DPN under low flow conditions. Both sDPN and rDPN were not able to cross the endothelial layer, even following Mannitol or Lexiscan treatment (Fig. 5**C**). Specifically, in the absence of HUVEC, the permeability values were equal to 0.019 ± 0.002 μm/sec and 0.014 ± 0.001 μm/sec (p = 0.595) for the sDPN and rDPN, respectively. After the inclusion of endothelial cells, the vascular permeability reduced further falling in the range of 0.007 ± 0.001 μm/sec, with no significant difference between the two nanoconstructs. Treatments with Mannitol and Lexiscan did not enhance the permeation of DPN. Also, the 200 nm PB beads generally returned a vascular permeability about 2 orders of magnitude higher than that observed for DPN under all the tested conditions. Representative images for the different tested conditions are provided in Fig. 5**D-E** (with and without HUVEC) and **Supporting Fig. S5 and S6** (upon treatment with Mannitol and Lexiscan). Indeed, the permeability values documented in Fig. 5**C** were expected given the size of the discoidal nanoconstructs, which have been designed to target the malignant vasculature rather than extravasating at sites of vascular hyperpermeability [31,34].

Then, vascular adhesion experiments were performed under three different conditions: a low capillary flow condition (low flow), which is characterized by a flow rate of 0.1 μL/min (wall shear stress ~0.03 Pa; average velocity ~0.2 mm/s) as opposed to a physiological capillary flow condition (physiological flow), which is characterized by a flow rate of 0.5 μL/min (wall shear stress ~0.15 Pa; average velocity of ~1 mm/s); and an intermediate flow condition characterized by a flow rate of 0.25 μL/min (wall shear stress ~0.071 Pa; average velocity ~500 μm/s). Interestingly in the absence of HUVEC, DPN appeared to be attracted and entrapped at the micro-pillar membrane rather than adhering on the fibronectin-coated PDMS of the main channel (Fig. 6**A** and **Supporting Fig. S7,** sDPN – **left column**; rDPN – **right column**).

Note that the matrix filling the extravascular compartment would favor the formation of 'openings', similar to fenestrations in a malignant vasculature, at the micro-pillar interface where DPN could be trapped. The number of entrapped DPN grows with the flow rate for both the soft and rigid configurations. However, the soft DPN showed a stronger tendency than the rigid DPN to be entrapped at the micro-pillar interface forming almost a continuous layer of particles at the highest flow rates (Fig. 6**A**, **right column**). The bars in the chart of Fig. 6**B-C** return theamounts of adherent DPN, expressed in terms of fluorescent intensity, within the channel and at the micro-pillar interface, respectively, for the different tested flow rates.

In the presence of endothelial cells, a different behavior was observed. Under this condition, the micro-pillar membrane was no more an attractor for DPN as the vascular cells would prevent the formation of openings. Adhesion within the channel on the HUVEC was instead preferred by DPN (Fig. 6**D** and **Supporting Fig. S7,** sDPN – **left column**; rDPN – **right column**). Interestingly, the soft DPN were observed to adhere at low flow rates more than rigid DPN. The opposite trend was instead observed at the higher

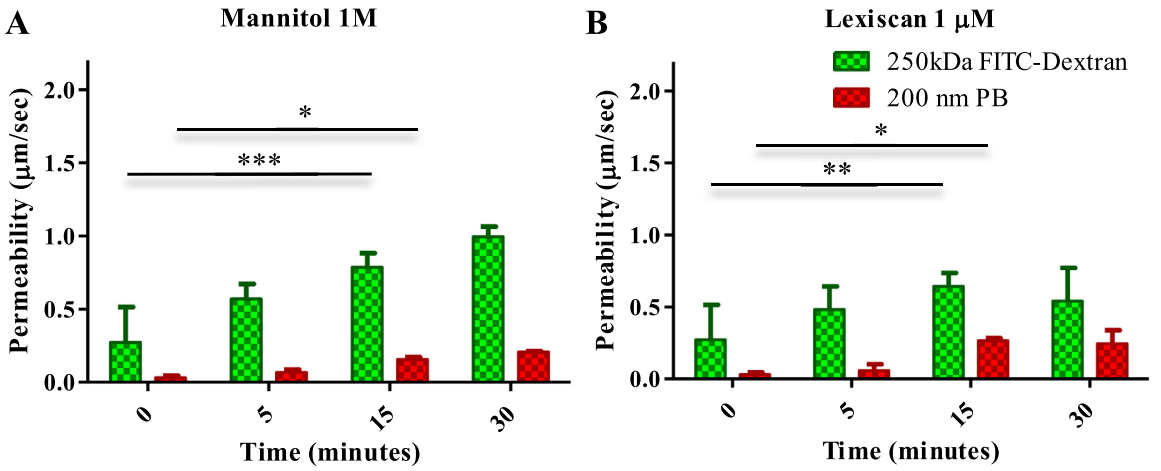

Time (minutes)	Mannitol 1M		Lexiscan 1µM	
	250kDa FITC-Dextran (µm/sec)	200 nm PB (µm/sec)	250kDa FITC-Dextran (µm/sec)	200nm PB (µm/sec)
0	0.27 ± 0.24	0.02 ± 0.01	0.27 ± 0.24	0.02 ± 0.01
5	0.56 ± 0.10	0.06 ± 0.02	0.48 ± 0.16	0.05 ± 0.04
15	0.78 ± 0.09	0.15 ± 0.01	0.64 ± 0.09	0.26 ± 0.01
30	0.99 ± 0.06	0.2 ± 0.006	0.54 ± 0.23	0.24 ± 0.09

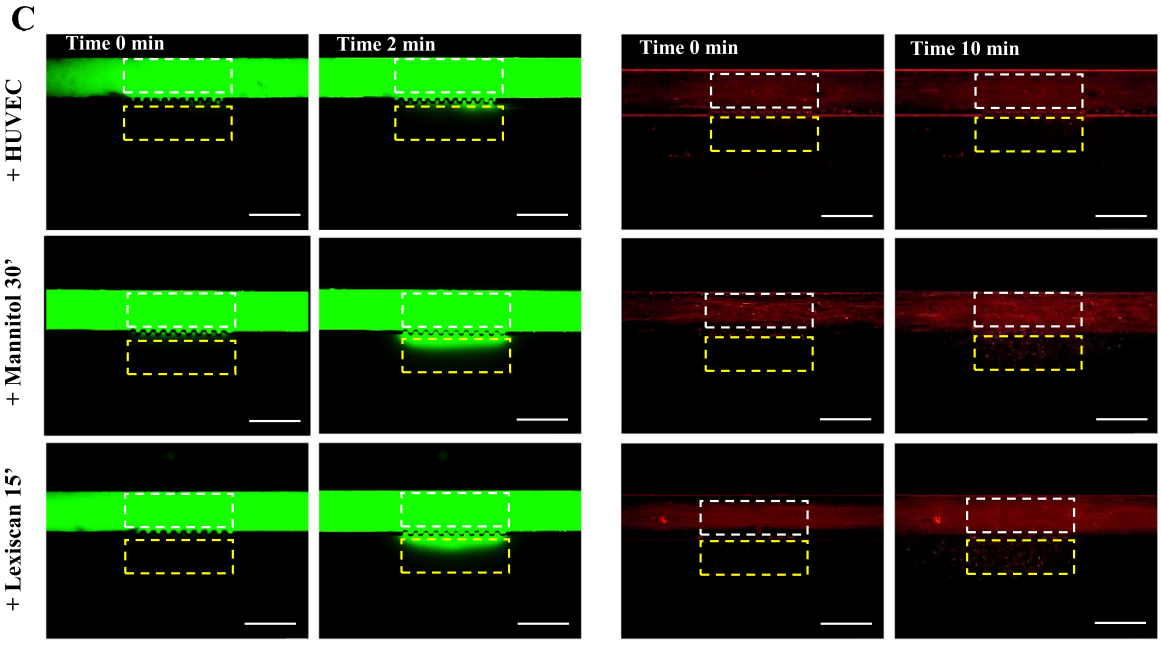

Fig. 4. Effect of permeabilizing agents. Permeability coefficients calculated for 250 kDa-FITC Dextran and 200 nm PB in a microfluidic device with HUVEC exposed to **(A)** 1 M Mannitol and **(B)** 1 µM Lexiscan. ($n \geq 5$) ($p < 0.05$ denoted with *, $p < 0.01$ denoted with **, $p < 0.001$ denoted with ***). Permeability values are presented in the table as average ± SD. **C.** Representative fluorescence images of 250 kDa-FITC Dextran (left) and 200 nm PB (right) permeation at 0.1 µL/min across the micro-pillar membrane under normal conditions (top row), after 30 min treatment with 1 M Mannitol (intermediate row), and 15 min treatment with 1 µM Lexiscan (bottom row) (Scale bar: 250 µm).

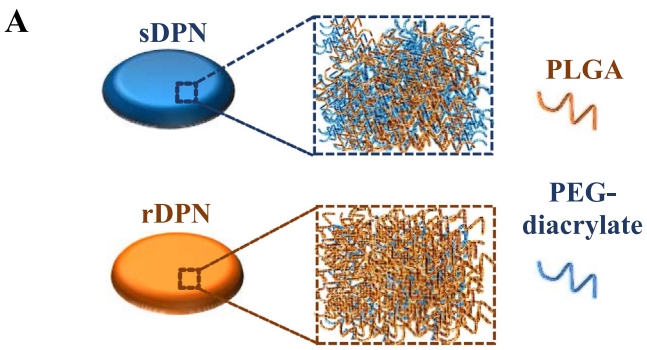

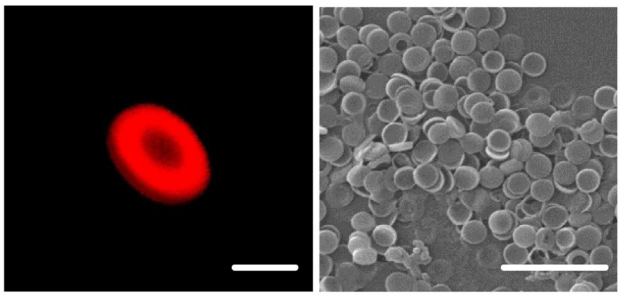

C

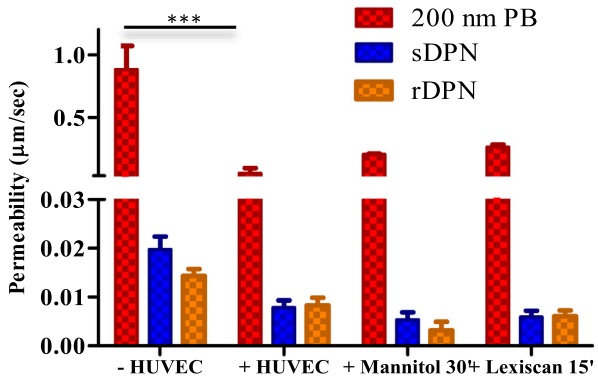

	200 nm PB (µm/sec)	sDPN (µm/sec)	rDPN (µm/sec)
-HUVEC	0.88 ± 0.18	0.019 ± 0.002	0.014 ± 0.001
+ HUVEC	0.05 ± 0.04	0.007 ± 0.001	0.008 ± 0.001
+ Mannitol	0.2 ± 0.006	0.005 ± 0.004	0.003 ± 0.002
+ Lexiscan	0.26 ± 0.01	0.005 ± 0.003	0.006 ± 0.001

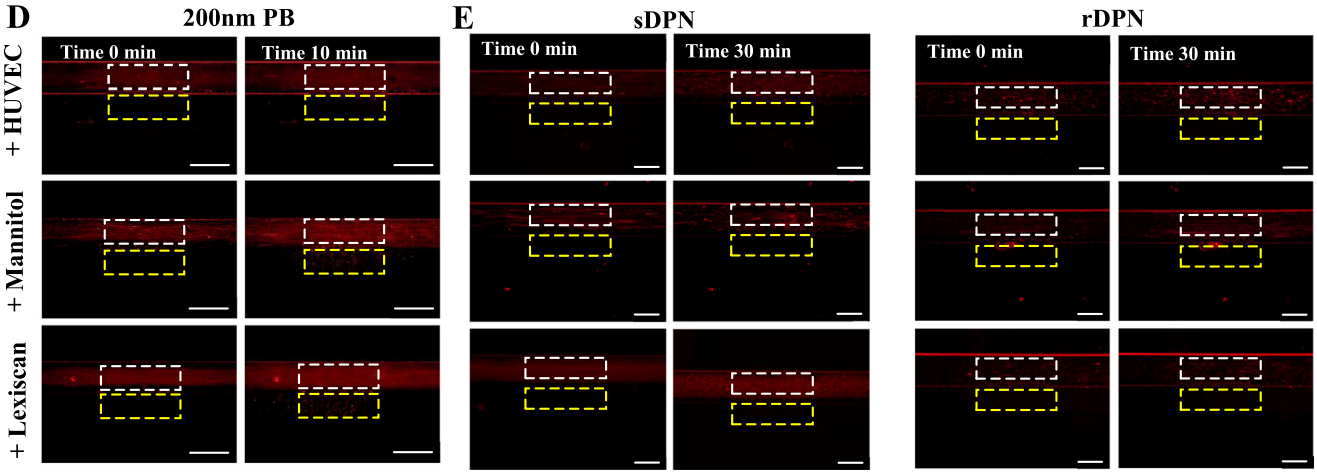

Fig. 5. Vascular permeability of polymeric nanoconstructs. **A.** Schematic illustration of sDPN (blue) and rDPN (orange) resulting from the mixing of PLGA and PEG-DA chains. **B.** Confocal image (left) and scanning electron micrograph (right) of DPN (Scale bar: 1 µm (left), 5 µm (right)). **C.** Permeability coefficients calculated for 200 nm PB, soft DPN (sDPN) and rigid DPN (rDPN) in the absence of HUVEC (−HUVEC), with HUVEC (+HUVEC), with HUVEC treated with 1 M Mannitol for 30 min (+Mannitol 30 min), and with HUVEC treated with 1 µM Lexiscan for 15 min (+Lexiscan 15 min). ($n \geq 5$). ($p < 0.001$ denoted with ***). **D.** Representative fluorescence images of 200 nm Polystyrene Beads diffusion at 0.1 µL/min with untreated HUVEC, after 30 min treatment of Mannitol and after 15 min treatment of Lexiscan (Scale bar 250 µm). **E.** Representative fluorescence images of sDPN (left) and rDPN (right) diffusion at 0.1 µL/min with untreated HUVEC, after 30 min treatment of Mannitol and after 15 min treatment of Lexiscan (Scale bar 250 µm). (For interpretation of the references to color in this figure legend, the reader is referred to the web version of this article.)

flow rates. This is summarized in the bar chart of Fig. 6**E**. Under low flow conditions, a fluorescence intensity value equal to 43 ± 9.35 AU was measured for sDPN as opposed to 23 ± 5.77 AU for rDPN ($p = 0.0006$). Under physiological flow conditions, adhering rDPN were associated to a fluorescence intensity of 44 ± 2.8 AU while for the sDPN the value was almost two times lower 26 ± 6.0 AU ($p = 0.004$) (Fig. 6**E**). Under intermediate flow conditions, sDPN and rDPN displayed no difference in vascular adhesion documenting a smooth transition from low to high flow rate conditions.

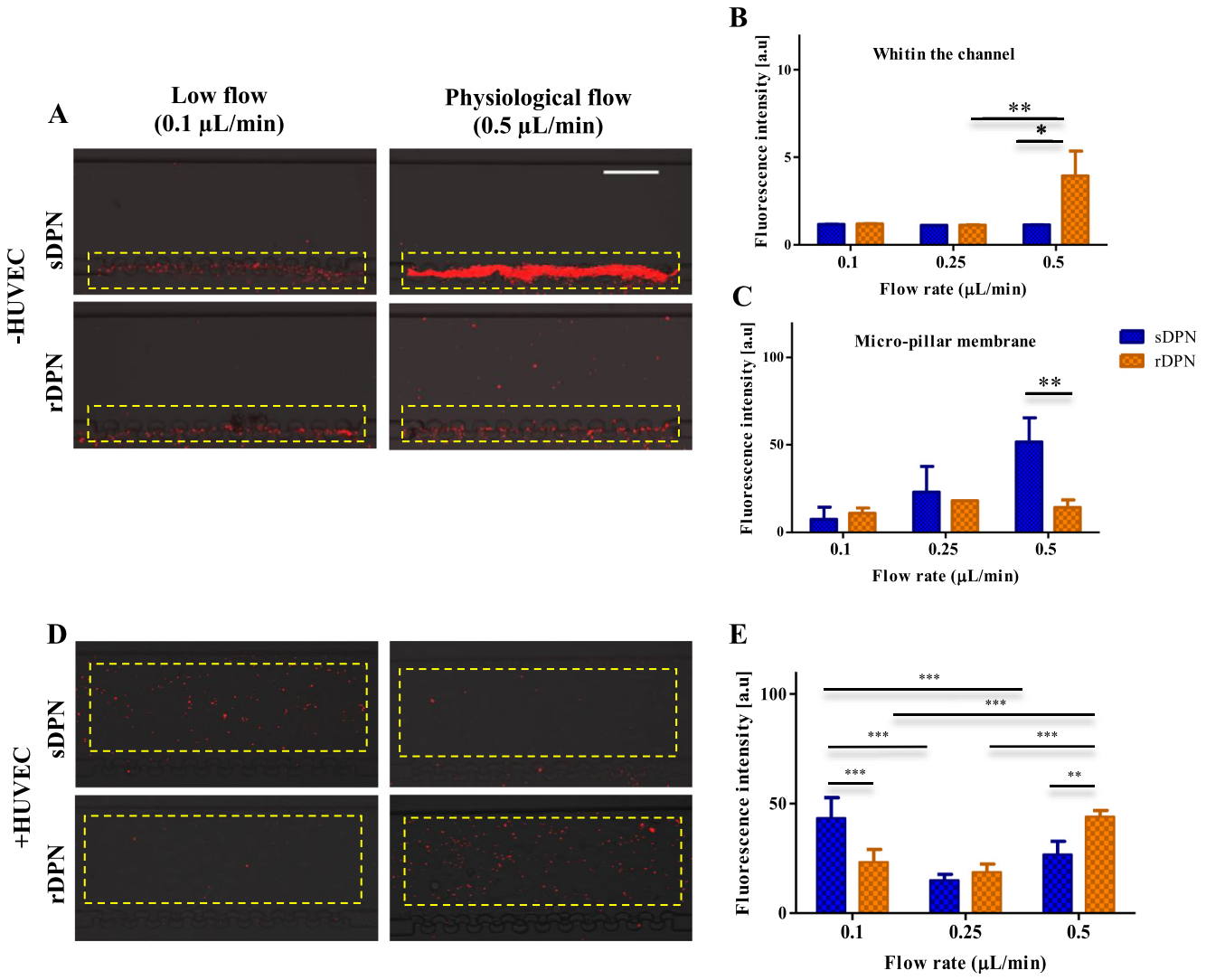

Fig. 6. Vascular dynamics of soft DPN versus rigid DPN. **A.** Representative images for the perivascular accumulation of sDPN and rDPN in a microfluidic device in the absence of HUVEC at low (0.1 µL/min) and high (0.5 µL/min) flow rates. **B.** Vascular adhesion of sDPN and rDPN within the channel under different flow conditions (−HUVEC). **C.** Entrapment of sDPN and rDPN at the micro-pillar membrane under different flow conditions (−HUVEC). **D.** Representative images of sDPN and rDPN firmly adhering in a microfluidic device with HUVEC at low (0.1 µL/min) and high (0.5 µL/min) flow rates. **E.** Vascular adhesion of sDPN and rDPN within the channel under different flow conditions (+HUVEC). ($n \geq 5$). ($p < 0.05$ denoted with *, $p < 0.01$ denoted with **, $p < 0.001$ denoted with ***).

4. Discussion

In drug delivery and biomedical imaging, systemically administered molecules and nanomedicines must either escape the vascular compartment and distribute within the diseased tissue (tissue targeting) or firmly adhere to the diseased vasculature (vascular targeting) in order to properly exert their curative and diagnostic functions. This process is strictly regulated by several factors including the local hydrodynamic conditions and vascular permeability. As such, assessing the efficacy of drug delivery systems *in vitro* requires the design and realization of microfluidic devices where flow rates and vascular permeability can be accurately and independently modulated reproducing physiological and pathological conditions. This need has inspired the engineering of a double-channel microfluidic device (Fig. 1) that integrates a vascular compartment and an extravascular chamber. The vascular compartment, with a width of 200 µm and a height of 50 µm, matches the characteristic dimensions of arterioles and large capillaries and was coated by endothelial cells [43,44]. For the extravascular compartment, a mixture of collagen type I and Matrigel led to the realization of a biologically inspired ECM (Fig. 2) [45,46]. The extracellular matrix underlying the vascular endothelium provides simultaneously a mechanical function, supporting the blood vessel walls, and a biological function, mediating signals involved in endothelial cell proliferation, migration, morphogenesis, survival, and angiogenesis. This is achieved by multiple properly mixed components, including collagen I, III and IV, different laminin types, perlecan and other less abundant proteins and fibers. Matrigel© is rich in laminin, collagen type IV, and perlecan, thus approximating the composition of the vascular basement membrane [47]. This observation triggered the authors to use a mixture of collagen type I and Matrigel to fill up the space next to the vascular endothelium within the double-cannel system.

Seven different collagen/Matrigel combinations were considered and characterized for their permeability, as documented in Fig. 2. The combination 80% of collagen and 20% of Matrigel returned physiologically relevant permeabilities to 250 kDa FITC-Dextran molecules. This ratio was used and recommended in the work by Wimmer and colleagues for generating blood vessel organoids [48]. Specifically, in this Nature Protocol work, 2 mg/mL of

Collagen type I was mixed with Matrigel in a 4:1 ratio, which is corresponding to the 80:20 ratio used in the current work. Higher Matrigel concentrations were, with 50:50 or even 25:75 ratios, were also documented in the literature but mostly for replicating the malignant extracellular matrix, as reported in Anguiano and colleagues [49]. Indeed, high Matrigel concentrations return matrices that are excessively impermeable to molecules and cells, whereas a 100% collagen type I matrix would have lacked collagen type IV, laminin and other fiber and proteins that are contained in Matrigel as well as in the vascular basement membrane.

With such a system, first, the formation of a continuous endothelial barrier in the vascular compartment was assessed using electron microscopy, to demonstrate the assembly of a confluent endothelial barrier (Fig. 1**C** and **Supporting Information**); confocal fluorescent microscopy, to document the expression of VE-cadherin molecules (Fig. 1**D** and **Supporting Information**); and dynamic assays to quantify the vascular permeability of 250 kDa Dextran molecules and 200 nm polystyrene beads (Fig. 2**D**). The molecular Dextran 250 kDa has a characteristic hydrodynamic diameter of ~10 nm and, as such, represents the boundary between small molecules ($\ll$ 10 nm), which can easily permeate even continuous vascular walls (except for the blood brain barrier) and macromolecules/nanoparticles ($\gg$ 10 nm), which can only permeate discontinuous, fenestrated, and unhealthy vascular walls. This was then the main rationale to consider Dextran 250 kDa rather than smaller Dextran molecules that would fall in the small molecule regime.

The proper deposition and culturing of HUVEC within the microfluidic device prompted the formation of a continuous endothelial layer on the micro-pillar membrane leading to permeability values as low as 0.93 ± 0.30 μm/sec for the 250 kDa Dextran molecules and 0.04 ± 0.005 μm/sec for the larger 200 nm polystyrene beads. The vascular permeability for the macromolecules (250 kDa Dextran molecules ~10 nm particles) was further reduced to 0.27 ± 0.24 μm/sec upon exposing the endothelial cells to db-cAMP (Fig. 3). The treatment of the endothelial cells first with cAMP and then with the clinically relevant vasodilators, Mannitol and Lexiscan, has the objective of documenting the versatility of the proposed system and demonstrate that it is capable to reproduce "healthy" and hyper-permeable blood vessel walls. However, the term "healthy" should be properly contextualized here as the objective of the work is to present a system for studying the vascular and perivascular dynamics of macromolecules and nanoparticles, as already specified in the title.

Indeed, the data in Fig. 3**A** do demonstrate that the pre-treatment with cAMP reduces the permeability to Dextran 250 kDa by 3 times as compared to untreated HUVECs. Notably, the same data show that the pre-treatment has no effect on the vascular permeability of the 200 nm PB. This confirms that the sole presence of HUVEC, with or without cAMP pretreatment, are sufficient to realize a "healthy" vasculature in the nanoparticle regime ($\gg$ 10 nm), while cAMP is needed for the 250 kDa macromolecule. Possibly, additional changes could be required to seal even more the vascular walls in the small molecule regime. But this falls outside the current scope of the work and will be certainly the topic of future works with the presented system.

These permeability values are in line with those documented for other vascular microfluidic platforms [50-53] and only slightly higher than those measured *in vivo* in the case of macromolecules [54]. Indeed, the current microfluidic device configuration includes only a layer of endothelial cells without perivascular supportive cells, such as pericytes, smooth muscle cells, and fibroblasts that would reduce further the vascular permeability [55,56]. Furthermore, the human umbilical vascular endothelial cells (HUVECs) used in this work typically line the walls of the macrovasculature and are intrinsically more permeable than microvascular cells, such as human dermal blood microvessels (BECs) or brain microvascular endothelial cells (BMECs). Finally, the sustained flow in authentic blood vessels 'massage' the endothelial monolayer favoring cell–cell interaction and reducing permeability. Cell type and spatial organization, the basal lamina and extracellular matrix composition and architecture as well as blood flow contribute all together, directly and indirectly, to modulate the permeability and biomechanical response of the endothelium.

Despite this, it should be highlighted that the treatment with db-cAMP did not affect the permeability for the 200 nm particles, suggesting that the proposed endothelial barrier could be accurately and efficiently employed to study the vascular transport of nanoparticles. The ability to modulate the vascular permeability was demonstrated further by infusing directly into the microfluidic devices Mannitol and Lexiscan. The exposure of the otherwise continuous endothelial layer to these permeabilizing agents results in an increase in permeability for both Dextran molecules and, at a lower extent, the 200 nm polystyrene beads (Fig. 4 and **Supporting Information**).

After demonstrating the ability to precisely dial the vascular permeability from physiological to pathological values, the microfluidic device was used to study the dynamics of blood borne polymeric nanoconstructs. The largest majority of man-made nanoparticles for drug delivery and biomedical imaging have a spherical shape and a characteristic hydrodynamic size ranging from several tens of nanometers up to a few hundreds of nanometers [57]. Upon systemic administration, these systems are transported by the blood flow along the circulatory system and progressively deposit in tissues that are characterized by a discontinuous endothelium. These include cancer, whose neovasculature is characterized by intracellular openings – fenestrations – as large as a few microns [12], but also healthy filtering organs, such as the liver and spleen, where the vascular endothelium is naturally discontinuous. Therefore, the 200 nm polystyrene beads (PB) were selected to represent conventional nanomedicines that would accumulate into malignant tissues exploiting the enhanced permeation and retention (EPR) effect. The Discoidal Polymeric Nanoparticles (DPN) have been designed to navigate the circulatory system more efficiently than spherical nanoparticles and accumulate in the diseased vasculature without relying on the EPR effect [33,34]. Importantly, the size, shape, surface properties and mechanical stiffness of this injectable drug delivery system can be optimized to modulate uptake by cells of the immune system [31,32]. In this work, two configurations of DPN were considered in a first attempt to elucidate the role of particle deformability in vascular transport and adhesion. Specifically, soft (sDPN) and rigid (rDPN) discoidal particles were employed. In this work, we observed sDPN accumulating more than rDPN at vascular interfaces characterized by an irregular geometry and low blood velocity. These are indeed conditions that differentiate tortuous, low perfused malignant blood vessels versus their regular healthy counterparts.

Specifically, in addition to the commercially available 200 nm polystyrene beads (PB), soft and rigid 1,000 × 400 nm discoidal polymeric particles (DPN) were considered. It is here important to recall that while conventional nanoparticles, with a characteristic size of 100 – 200 nm, are expected to cross the hyperpermeable endothelial layer, DPN were designed to drift across the streamlines, in a process known as margination; firmly stick to the diseased vasculature; and release thereof their therapeutic cargo and imaging signal [34]. In this context, the microfluidic device was used to evaluate the ability of soft and rigid DPN to marginate and adhere to the endothelial barrier under different flow and permeability conditions. In particular, the DPN behavior was tested at flow rates ranging from 0.1 μL/min (~100 μm/s), mimicking sub-physiological, quasi-tumoral flow conditions, to 0.5 μL/min (~1

mm/s), reproducing more physiologically relevant flow conditions [36]. As expected, neither the sDPN nor the rDPN were able to cross the micropillar membrane and diffuse deep into the extravascular compartment.

In the absence of endothelial cells, all the walls of the microfluidic device were solely coated by a layer of fibronectin and appeared as relatively flat interfaces. Differently, however, the micro-pillar membrane zone appeared as a wavy interface with repetitive valleys and crests, still coated by the fibronectin layer. In this configuration, both rDPN and sDPN were observed to preferentially accumulate at the micro-pillar membrane as opposed to the top, bottom, and lateral walls of the device (Fig. 6**A-C**). The number of entrapped rDPN was almost constant over a wide range of flow rates. Although, at higher flow rates, rDPN were also observed to adhere at the bottom of the device. Interestingly, sDPN were entrapped in the micro-pillar membrane at a much higher extent than rDPN, in a shear flow dependent manner (Fig. 6**C**). Also, differently from rDPN, no significant accumulation of sDPN was observed on the bottom of the device, even at higher flow rates (Fig. 6**B**). This preferential accumulation of DPN at the micro-pillar membrane, in the absence of endothelium, should be associated to the direct geometrical entrapment of those nanoconstructs moving in proximity of the irregular, wavy interface. Also, the deformable sDPN could be more easily entrapped, as opposed to their rigid counterpart, as the local shear rate increases. However, this could only partially explain the dramatic difference observed when comparing soft versus rigid DPN (Fig. 6**C**). Possibly, an additional contribution to sDPN accumulation could derive by a direct, hydrodynamic-based attraction of these nanoconstructs to the micro-pillar membrane. While it is well known that deformable particles moving in proximity of a flat wall would tend to be pushed towards the center of the channel by dominating lift forces [58], only recently computational analyses have demonstrated that deformable particles moving in proximity of a wavy interface could migrate away from the center toward the wall [59]. This hydrodynamic-based attraction would depend on the amplitude ε of the wall waviness, the ratio between the wavelength λ and the characteristic size R of the particle, and the local flow conditions. Importantly, this hydrodynamic-based attraction would only apply to deformable particles. Indeed, only an *ad hoc* computational analysis accounting for the specific micro-pillar membrane geometry, flow conditions and particle properties could help evaluate the relative importance of hydrodynamic-based attraction over geometrical entrapment.

For an endothelialized vascular compartment, the waviness of the micro-pillar membrane is massively reduced and DPN geometrical entrapment cannot occur anymore (Fig. 6**D**). Notice, incidentally, that this is an additional demonstration of the proper endothelial coating of the micro-pillar membrane. Under this condition, the top, bottom, and lateral walls of the device form a continuous monolayer with a moderate waviness whose amplitude is now related to the cell nuclei. For the soft DPN, hydrodynamic-based attraction would be minimal and could outperform lift forces at the wall only at low flow velocities. This could explain the higher deposition observed for the sDPN at low flow rates (Fig. 6**E**). For the rigid DPN, the margination velocity would tend to grow with the flow rates thus explaining the larger particle deposition at higher flow velocities [60]. Even in this case, only an *ad hoc* computational analysis could help to univocally identify the governing mechanisms regulating the behavior of different DPN. However, this is beyond the scope of the current work and certainly constitutes the starting point for future studies on vascular dynamics of soft versus rigid, non-spherical particles.

5. Conclusions

A double-channel microfluidic device was demonstrated to study the transport of macromolecules and nanoconstructs under different vascular conditions. A vascular compartment was covered by a continuous layer of endothelial cells, whereas an extravascular chamber was filled with a mixed collagen-matrigel matrix. After demonstrating the integrity of the endothelial barrier using different complementary techniques, the vascular permeability of macromolecules (250 kDa FITC-Dextran), nanoparticles (200 nm polystyrene beads), and polymeric nanoconstructs (1,000 $\times$ 400 nm discs) was characterized under physiological and pathological conditions. First, it was shown that the proposed microfluidic device can replicate physiologically relevant values of permeability down to the order of 0.1 μm/sec for the ~10 nm Dextran macromolecules. Then, it was documented that the vascular permeability could be modulated, and specifically increased, by using two clinically relevant agents, Mannitol and Lexiscan. Finally, it was observed that soft discoidal polymeric nanoconstructs can more efficiently than their rigid counterparts adhere to the vascular walls under pathological vascular conditions. Collectively, these results demonstrate that the proposed double-channel microfluidic device could be efficiently and effectively used to test the vascular behavior of a variety of drug delivery systems under various conditions.

CRediT authorship contribution statement

Maria Grazia Barbato: Conceptualization, Methodology, Validation, Formal analysis, Investigation, Visualization, Data curation, Writing - original draft, Writing - review & editing. **Rui C. Pereira:** Conceptualization, Methodology, Supervision, Writing - review & editing. **Hilaria Mollica:** Conceptualization, Methodology, Supervision, Writing - review & editing. **AnnaLisa Palange:** Visualization, Supervision. **Miguel Ferreira:** Conceptualization, Methodology, Validation, Formal analysis, Validation, Writing - review & editing, Supervision. **Paolo Decuzzi:** Conceptualization, Methodology, Validation, Resources, Writing - review & editing, Visualization, Supervision, Project administration, Funding acquisition.

Declaration of Competing Interest

The authors declare that they have no known competing financial interests or personal relationships that could have appeared to influence the work reported in this paper.

Acknowledgments

This project was partially supported by the European Union's Seventh Framework Programme (FP7/2007-2013)/ERC grant agreement no. 616695; the European Union's Horizon 2020 Research and Innovation Programme under the Marie Sklodowska-Curie Grant Agreement no. 754490; and the Ministry of Foreign Affairs and International Cooperation with the Grant no. PGR00796.

Appendix A. Supplementary material

Supplementary data to this article can be found online at https://doi.org/10.1016/j.jcis.2021.03.053.

References

[1] M.K. Pugsley, R. Tabrizchi, The vascular system. An overview of structure and function, J. Pharmacol. Toxicol. Methods 44 (2) (2000) 333–340.

[2] Y. Komarova, A.B. Malik, Regulation of endothelial permeability via paracellular and transcellular transport pathways, Annu. Rev. Physiol. 72 (2010) 463–493.
[3] G.S. Offeddu et al., An on-chip model of protein paracellular and transcellular permeability in the microcirculation, Biomaterials 212 (2019) 115–125.
[4] B.T. Hawkins, T.P. Davis, The blood-brain barrier/neurovascular unit in health and disease, Pharmacol. Rev. 57 (2) (2005) 173–185.
[5] Y. Chen, L. Liu, Modern methods for delivery of drugs across the blood-brain barrier, Adv. Drug Deliv. Rev. 64 (7) (2012) 640–665.
[6] T. Patel et al., Polymeric nanoparticles for drug delivery to the central nervous system, Adv. Drug Deliv. Rev. 64 (7) (2012) 701–705.
[7] H.S. Choi et al., Renal clearance of quantum dots, Nat. Biotechnol. 25 (10) (2007) 1165–1170.
[8] S.M. Moghimi, A.C. Hunter, J.C. Murray, Long-circulating and target-specific nanoparticles: theory to practice, Pharmacol. Rev. 53 (2) (2001) 283–318.
[9] J.G. Schnitzler et al., Surmounting the endothelial barrier for delivery of drugs and imaging tracers, Atherosclerosis (2020).
[10] D. Aguilar-Cazares et al., Contribution of angiogenesis to inflammation and cancer, Front. Oncol. 9 (2019).
[11] R.K. Jain, Barriers to drug delivery in solid tumors, Sci. Am. 271 (1) (1994) 58–65.
[12] R.K. Jain, T. Stylianopoulos, Delivering nanomedicine to solid tumors, Nat. Rev. Clin. Oncol. 7 (11) (2010) 653–664.
[13] Y. Kim et al., Probing nanoparticle translocation across the permeable endothelium in experimental atherosclerosis, Proc. Natl. Acad. Sci. USA 111 (3) (2014) 1078–1083.
[14] J. Fang, H. Nakamura, H. Maeda, The EPR effect: Unique features of tumor blood vessels for drug delivery, factors involved, and limitations and augmentation of the effect, Adv. Drug Deliv. Rev. 63 (3) (2011) 136–151.
[15] A. Lee et al., Dexamethasone-loaded Polymeric Nanoconstructs for Monitoring and Treating Inflammatory Bowel Disease, Theranostics 7 (15) (2017) 3653–3666.
[16] S.A. Casnocha et al., Permeability of human endothelial monolayers: effect of vasoactive agonists and cAMP, J. Appl. Physiol. 67 (5) (1989) 1997–2005.
[17] B. Godin, E. Touitou, Transdermal skin delivery: predictions for humans from in vivo, ex vivo and animal models, Adv. Drug Deliv. Rev. 59 (11) (2007) 1152–1161.
[18] M. Islam, S. Beverung, R. Steward Jr, Bio-inspired microdevices that mimic the human vasculature, Micromachines 8 (10) (2017) 299.
[19] C.M. Sakolish et al., Modeling barrier tissues in vitro: methods, achievements, and challenges, EBioMedicine 5 (2016) 30–39.
[20] M.I. Bogorad et al., In vitro microvessel models, Lab Chip 15 (22) (2015) 4242–4255.
[21] M.E. Miali et al., Leaf-Inspired Authentically Complex Microvascular Networks for Deciphering Biological Transport Process, ACS Appl. Mater. Interfaces 11 (35) (2019) 31627–31637.
[22] C. Manneschi et al., A microfluidic platform with permeable walls for the analysis of vascular and extravascular mass transport, Microfluid. Nanofluid. 20 (8) (2016) 113.
[23] Y.T. Ho et al., A facile method to probe the vascular permeability of nanoparticles in nanomedicine applications, Sci. Rep. 7 (1) (2017) 1–13.
[24] H.-F. Wang et al., Tumor-vasculature-on-a-chip for investigating nanoparticle extravasation and tumor accumulation, ACS Nano 12 (11) (2018) 11600–11609.
[25] B. Zhang et al., Biodegradable scaffold with built-in vasculature for organ-on-a-chip engineering and direct surgical anastomosis, Nat. Mater. 15 (6) (2016) 669–678.
[26] K.M. Chrobak, D.R. Potter, J. Tien, Formation of perfused, functional microvascular tubes in vitro, Microvasc. Res. 71 (3) (2006) 185–196.
[27] G.M. Price, J. Tien, Subtractive methods for forming microfluidic gels of extracellular matrix proteins, in: Microdevices in biology and engineering, Artech House, Boston, MA, 2009, pp. 235–248.
[28] B. Kwak et al., Simulation of complex transport of nanoparticles around a tumor using tumor-microenvironment-on-chip, J. Control. Release 194 (2014) 157–167.
[29] Y. Tang et al., A biomimetic microfluidic tumor microenvironment platform mimicking the EPR effect for rapid screening of drug delivery systems, Sci. Rep. 7 (1) (2017) 1–14.
[30] H. Mollica et al., Two-channel compartmentalized microfluidic chip for real-time monitoring of the metastatic cascade, ACS Biomater. Sci. Eng. 5 (9) (2019) 4834–4843.
[31] J. Key et al., Soft Discoidal Polymeric Nanoconstructs Resist Macrophage Uptake and Enhance Vascular Targeting in Tumors, ACS Nano 9 (12) (2015) 11628–11641.
[32] R. Palomba et al., Modulating phagocytic cell sequestration by tailoring nanoconstruct softness, ACS Nano 12 (2) (2018) 1433–1444.
[33] M. Colasuonno et al., Erythrocyte-Inspired Discoidal Polymeric Nanoconstructs Carrying Tissue Plasminogen Activator for the Enhanced Lysis of Blood Clots, ACS Nano 12 (12) (2018) 12224–12237.
[34] A.L. Palange et al., Deformable Discoidal Polymeric Nanoconstructs for the Precise Delivery of Therapeutic and Imaging Agents, Mol. Ther. 25 (7) (2017) 1514–1521.
[35] M. Ferreira et al., Optimizing the Pharmacological Properties of Discoidal Polymeric Nanoconstructs Against Triple-Negative Breast Cancer Cells, Front. Bioeng. Biotechnol. 8 (5) (2020).
[36] G. Follain et al., Fluids and their mechanics in tumour transit: shaping metastasis, Nat. Rev. Cancer (2019) 1–18.
[37] N. Serna-Márquez et al., Fibrillar Collagen Type I Participates in the Survival and Aggregation of Primary Hepatocytes Cultured on Soft Hydrogels, Biomimetics 5 (2) (2020) 30.
[38] M. McRae et al., Characterization of cell-cell junction changes associated with the formation of a strong endothelial barrier, Tissue Barriers 6 (1) (2018) e1405774.
[39] E. Neuwelt et al., Osmotic blood-brain barrier disruption: a new means of increasing chemotherapeutic agent delivery, Trans. Am. Neurol. Assoc. 104 (1979) 256–260.
[40] R.S. D'Amico et al., Super selective intra-arterial cerebral infusion of modern chemotherapeutics after blood–brain barrier disruption: where are we now, and where we are going, J. Neurooncol. (2020) 1–18.
[41] S. Jackson et al., The effect of regadenoson-induced transient disruption of the blood–brain barrier on temozolomide delivery to normal rat brain, J. Neurooncol. 126 (3) (2016) 433–439.
[42] D.-G. Kim, M.S. Bynoe, A2A adenosine receptor regulates the human blood-brain barrier permeability, Mol. Neurobiol. 52 (1) (2015) 664–678.
[43] H.G. Augustin, G.Y. Koh, Organotypic vasculature: From descriptive heterogeneity to functional pathophysiology, Science 357 (6353) (2017).
[44] C.G. Ellis, J. Jagger, M. Sharpe, The microcirculation as a functional system, Crit. Care 9 (S4) (2005) S3.
[45] M.G. McCoy et al., Collagen I hydrogel microstructure and composition conjointly regulate vascular network formation, Acta Biomater. 44 (2016) 200–208.
[46] M. Anguiano et al., Characterization of three-dimensional cancer cell migration in mixed collagen-Matrigel scaffolds using microfluidics and image analysis, PLoS ONE 12 (2) (2017).
[47] G.E. Davis, D.R. Senger, Endothelial extracellular matrix: biosynthesis, remodeling, and functions during vascular morphogenesis and neovessel stabilization, Circ. Res. 97 (11) (2005) 1093–1107.
[48] R.A. Wimmer et al., Generation of blood vessel organoids from human pluripotent stem cells, Nat. Protoc. 14 (11) (2019) 3082–3100.
[49] M. Anguiano et al., The use of mixed collagen-Matrigel matrices of increasing complexity recapitulates the biphasic role of cell adhesion in cancer cell migration: ECM sensing, remodeling and forces at the leading edge of cancer invasion, PLoS ONE 15 (1) (2020) e0220019.
[50] S. Alimperti et al., Three-dimensional biomimetic vascular model reveals a RhoA, Rac1, and N-cadherin balance in mural cell–endothelial cell-regulated barrier function, Proc. Natl. Acad. Sci. 114 (33) (2017) 8758–8763.
[51] J.F. Wong et al., Integrated electrochemical measurement of endothelial permeability in a 3D hydrogel-based microfluidic vascular model, Biosens. Bioelectron. 147 (2020) 111757.
[52] I.K. Zervantonakis et al., Three-dimensional microfluidic model for tumor cell intravasation and endothelial barrier function, Proc. Natl. Acad. Sci. 109 (34) (2012) 13515–13520.
[53] Y. Zheng et al., In vitro microvessels for the study of angiogenesis and thrombosis, Proc. Natl. Acad. Sci. 109 (24) (2012) 9342–9347.
[54] C. Michel, F. Curry, Microvascular permeability, Physiol. Rev. 79 (3) (1999) 703–761.
[55] N.J. Abbott, L. Rönnbäck, E. Hansson, Astrocyte–endothelial interactions at the blood–brain barrier, Nat. Rev. Neurosci. 7 (1) (2006) 41.
[56] M. Campisi et al., 3D self-organized microvascular model of the human blood-brain barrier with endothelial cells, pericytes and astrocytes, Biomaterials 180 (2018) 117–129.
[57] J. Shi et al., Cancer nanomedicine: progress, challenges and opportunities, Nat. Rev. Cancer 17 (1) (2017) 20.
[58] T.W. Secomb, Mechanics of blood flow in the microcirculation, Symp. Soc. Exp. Biol. 49 (1995) 305–321.
[59] M. Laumann et al., Emerging attractor in wavy poiseuille flows triggers sorting of biological cells, Phys. Rev. Lett. 122 (12) (2019) 128002.
[60] S.Y. Lee, M. Ferrari, P. Decuzzi, Shaping nano-/micro-particles for enhanced vascular interaction in laminar flows, Nanotechnology 20 (49) (2009) 495101.